




 Cite this: *Analyst*, 2022, **147**, 5607

 Received 14th October 2022,
 Accepted 12th November 2022
 DOI: 10.1039/d2an01684b

rsc.li/analyst

Hyperpolarized ^{29}Si magnetic resonance spectroscopy of selectively radical-embedded silica nanoparticles†

 Quy Son Luu,^{‡a} Quynh Thi Nguyen,^{‡b} Jiwon Kim,^{‡a} Jeunghwan Kim,^b Uyen Thi Do,^a Nicholas Whiting,^c Jeong Hyun Shim,^{*d} Sun-Joon Min ^{*a,b} and Youngbok Lee ^{*a,b}

The embedding of radicals at different locations within core@shell silica nanoparticles contributes to enhanced polarization capability and can be self-polarized without adding external radicals. With grafting the radical source homogeneously inside of the nanoparticles, a significant ^{29}Si hyperpolarization signal enhancement of 49.4 was obtained.

Magnetic resonance imaging (MRI) has emerged as one of the most powerful clinical tools for both functional and physiological imaging. Owing to the advancement of this diagnostic tool, the use of MRI molecular probes that enable the production of a specific signal with high image contrast has significantly increased in recent years.¹ Typically, imaging probes devised from low-sensitivity nuclei (^{13}C , ^{15}N , and ^{29}Si)-based materials^{2–4} have been developed using hyperpolarization techniques, such as dynamic nuclear polarization (DNP).⁵ Among them, hyperpolarized ^{29}Si has emerged as a promising candidate for MRI applications owing to the high biocompatibility and biodegradability of Si and its oxide derivatives and the presence of extremely low amounts of Si in the human body.⁶ Recently, background-free positive-contrast imaging using hyperpolarized Si particles has been achieved *in vivo* using ^{29}Si MRI.^{4,7} Interestingly, hyperpolarized Si nanoparticles exhibit long ^{29}Si hyperpolarization spin-lattice relaxation times (T_1) of over 40 min, enabling an extended imaging

timeframe, thereby facilitating Si particles as ideal MRI contrast agents.^{4,8–10} However, the development of silicon nanoparticles for MRI applications is limited by certain challenges, including their morphology and size control, dispersibility, and surface modifications. The synthesis of monodispersed spherical Si particles within the *in vivo* applicable size range,¹¹ particularly 20–100 nm, is extremely challenging using both chemical and physical approaches.¹² In addition to morphology and size control issues, several fabrication techniques result in Si nanoparticles that are hydrogen-terminated and possess poor water dispersion, thus limiting their biological applications.¹³ Furthermore, the unfeasible large-scale synthesis of silicon nanoparticles also becomes a challenge for their applications.

Silica nanoparticles (SiO_2 NPs) are prospective materials for addressing the shortcomings of Si NPs as hyperpolarized ^{29}Si imaging probes because of their favorable dispersion, biocompatibility, easily tunable size, facile surface modification and feasible large-scale production.^{14–16} However, SiO_2 NPs lack endogenous radicals, whereas dynamic nuclear polarization requires free electrons to generate high electron-spin polarization, which is then transferred to ^{29}Si nuclei *via* dipolar interactions and enhances ^{29}Si nuclear spin polarization.^{17,18} To overcome this drawback, several studies have used organically modified silica (ORMOSIL) materials with radicals.¹⁹ However, these studies did not employ spherical and monodispersed SiO_2 NPs, and the samples could only be partially polarized.²⁰ Herein, we developed radical-embedded SiO_2 NPs in which modified 2,2,6,6-tetramethylpiperidine-1-oxyl (TEMPO) acted as an internal electron-spin source for hyperpolarization during DNP. In particular, we synthesized radical-embedded SiO_2 NPs using tetraethyl orthosilicate (TEOS) and 1-[3-(triethoxysilyl)propyl]-3-[4-(2,2,6,6-tetramethylpiperidine-1-oxyl)]urea (TEOS-TEMPO) through the Stöber method and ORMOSIL NP approach (Scheme 1). To determine the ideal radical-enriched structures for DNP signal amplification, homogeneously embedded (HOMO), selectively core-embedded (CORE), selectively shell-embedded (SHELL) SiO_2

^aDepartment of Bionano Technology, Center for Bionano Intelligence Education and Research, Hanyang University, Ansan 15588, South Korea.

E-mail: yblee@hanyang.ac.kr

^bDepartment of Applied Chemistry, Hanyang University, Ansan 15588, South Korea.

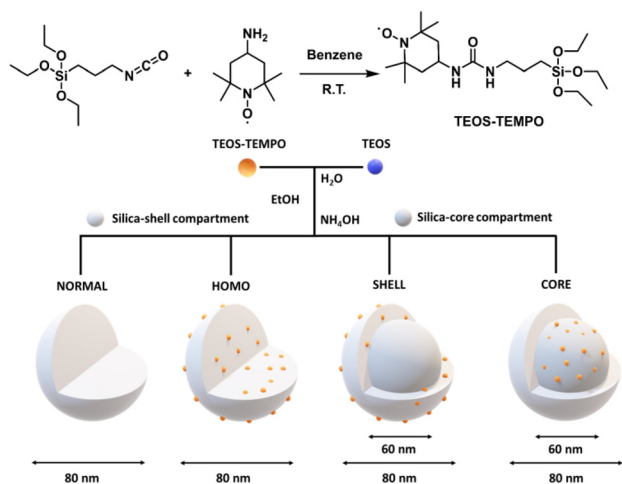
E-mail: sjmin@hanyang.ac.kr

^cDepartment of Physics & Astronomy and Department of Biological & Biomedical Sciences, Rowan University, Glassboro, NJ 08028, USA

^dQuantum magnetic imaging team, Korea Research Institute of Standards and Science, Daejeon 34113, South Korea. E-mail: jhshim@kriss.re.kr

† Electronic supplementary information (ESI) available: Synthesis and characterization, dynamic light scattering spectra, scanning electron microscopy, and simulation data analysis. See DOI: <https://doi.org/10.1039/d2an01684b>

‡ These authors contributed equally to this work.



Scheme 1 Schematic illustration of synthetic processes for TEOS-TEMPO, and radicals embedded silica nanoparticles.

NPs, and control sample without internal radicals (NORMAL) were prepared and tested.

To study the characteristics of TEMPO-embedded silica NPs and the preferred TEMPO distribution for signal amplification using DNP, both homogeneous and selectively TEMPO-enriched core@shell silica NPs with similar concentrations of radicals were investigated. Herein, we synthesized 80 nm non-porous spherical silica particles using the Stöber method, and the same amounts of TEMPO-TEOS were selectively used (along with the commercial TEOS precursor) for the radical-enriched samples. While homogeneous TEMPO-embedded (HOMO) silica NPs were prepared using one-pot synthesis, the two-step synthetic procedure was utilized for core@shell samples in which 60 nm silica cores were synthesized first, followed by the formation of a 10 nm shell in the second step. Here, TEMPO-TEOS was selectively added during core preparation for core-only radical-enriched (CORE) samples or in the shell creation stage for the shell-only radical-enriched (SHELL) samples. Additionally, for the control sample, we also synthesized 80 nm silica NPs using only commercial TEOS *via* a one-pot synthesis (NORMAL). Owing to the difference in the structures of the silica samples and the necessity of verifying the impact of the embedded TEMPO, we performed dynamic light scattering (DLS) and scanning electron microscopy (SEM) to characterize the particle size distribution and morphology of each silica set. From the SEM results provided in Fig. 1 and Table S1,[†] monodisperse SiO₂ nanoparticles with a size of approximately 80 nm were observed for both NORMAL and TEMPO-embedded silica samples. The high monodispersity of the silica samples was confirmed *via* DLS measurements, which demonstrated a polydispersity index of approximately 0.07–0.13 (Fig. S1 and Table S1[†]). For CORE and SHELL samples, after the coating step, the particle size increases from 58.0 ± 4.9 to 78.5 ± 6.9 nm and 62.5 ± 4.6 to 80.9 ± 5.6 nm, respectively, (Table S1[†]), indicating that the shell component of the core-shell particles were approximately 10 nm in thick-

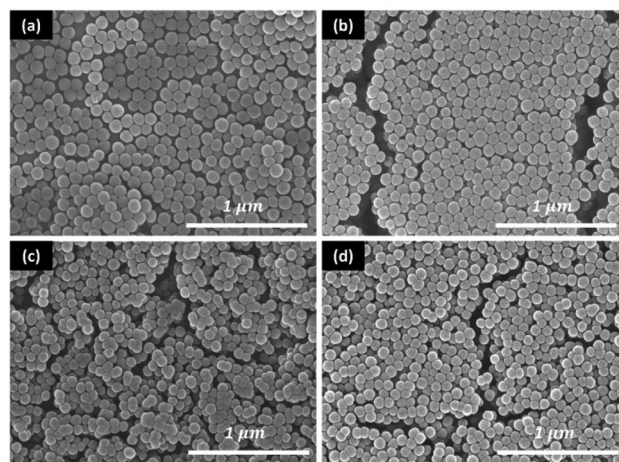


Fig. 1 Scanning electron microscopy (SEM) images of (a) NORMAL, (b) HOMO, (c) CORE, and (d) SHELL samples.

ness. All particles exhibited a smooth surface and spherical shape; hence, TEMPO addition or structural differences did not cause any changes in the particle morphology and size.

In addition to morphological characterization, we also evaluated the internal structures of the silica particles (with and without embedded radicals) using ²⁹Si solid-state nuclear magnetic resonance (²⁹Si SS-NMR). Two different resonance signals that correspond to the surface silicon sites, monohydroxy terminated Q₃ (Si(OSi≡)₃OH) and sub-surface site non-hydroxy terminated Q₄ (Si(OSi≡)₄), at approximately –100 and –110 ppm, respectively, were observed in all samples (Fig. 2).²¹ The fractions of Q_n sites for the samples were determined using the deconvoluted Gaussian peak areas in high-power decoupling (HPDEC) ²⁹Si SS-NMR spectra, which are shown as multicolor curves in Fig. 2 (fitted by OriginLab Corporation,

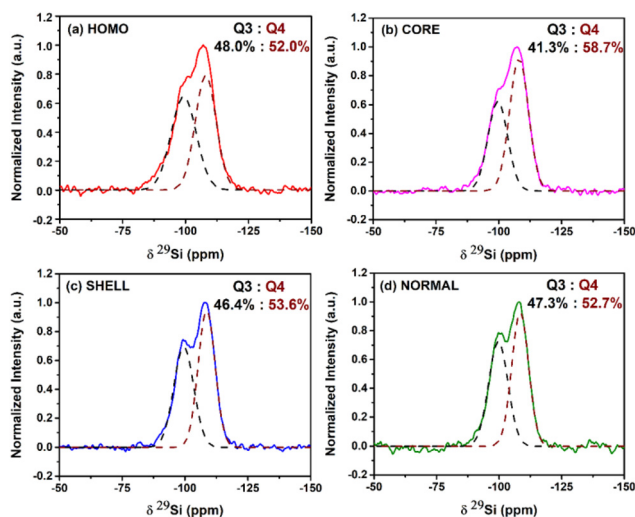


Fig. 2 Deconvolution of HPDEC ²⁹Si SS-NMR of (a) HOMO, (b) CORE, (c) SHELL, and (d) NORMAL samples.

MA, USA). Based on the calculated results, the Q_4/Q_3 intensity ratios for all samples were relatively similar, with ratios of 1.1 for the NORMAL and 1.1, 1.2, and 1.4 for the HOMO, SHELL, and CORE silica samples, respectively (Table S2[†]). Because of the differing locations of the radicals embedded within the nanoparticle of each sample, the surface site in SHELL nanoparticles and the sub-surface site in CORE cases become broader than those in the NORMAL case. On the other hand, due to the existence of radicals homogeneously inside particles, wider Q_3 and Q_4 sites are both observed in HOMO sample spectrum. Although the linewidth of TEMPO-enriched samples was slightly broader than that of NORMAL samples (Fig. 2 and Table S2[†]) owing to the paramagnetic effect of TEMPO-embedded radicals, the small amounts of embedded TEMPO did not induce noticeable structural differences in the SiO_2 NPs.

In addition, electron paramagnetic resonance (EPR) analysis was used to obtain more information about the electron spin states of the SiO_2 NPs. The line shapes of the TEMPO-enriched and NORMAL silica particles are clearly differentiated, as shown in the EPR spectra in Fig. 3. While multi-peak spectra were observed for the HOMO, CORE, and SHELL samples, NORMAL sample demonstrated a background-like EPR spectrum due to lacking internal radicals. The results can be explained by the EPR signal arises from the electron Zeeman interaction and the hyperfine interaction then causes the splitting into an equal intensity triplet; however, hyperfine anisotropy may contribute to the dominant effect for observing line shape of organic radical at X-band frequencies in the solid state.²² In particular, the electron Zeeman interaction (H_{EZ}) is occurred between the unpaired electron and the magnetic field.²³ While the electron-nuclear hyperfine interaction (H_{HF}) is between unpaired electron ($S = 1/2$) and ^{14}N nucleus ($I = 1$) of the nitroxide group (N-O^\bullet).^{22,23} Furthermore, the H_{EZ} and H_{HF} interactions are described by the g and A tensors, respectively (see Table S3[†]). The g tensor is a fingerprint of electron

environment, which consistent to chemical shift in NMR; while the A tensor is similar to dipole-dipole interaction of nuclear spin in NMR.²² According to the estimated results, three different values were obtained for the g tensors for all samples, in which g_x , g_y , and g_z were approximately 2.003, 2.001, and 1.998, respectively. The as-determined g tensor values were consistent with and those previously reported for nitroxide radicals, and the g -factor ($g_x \neq g_y \neq g_z$) is rhombic due to the structure of the nitroxide moiety.²² In terms of the A tensor, three distinct values of A_x , A_y , and A_z were obtained *via* hyperfine splitting from the TEMPO-embedded samples because the tumbling is extremely slowed in a solid, the anisotropic spectrum is observed.²² The A tensor values of three embedded radical sample are similar to previously reported literature,^{22,24} such as $A_x = 6.2$ G, $A_y = 11.5$ G, and $A_z = 37.0$ G. The A_z is much higher than A_x and A_y due to the magnetic field is parallel to the z -axis (parallel to $2p_z$ orbital of nitrogen atom) and the x -axis parallel to the N-O^\bullet bond.²⁴ Hence, the high field transition shift to higher field, consequently, the A_z has largest value and g_z has smallest value as mentioned above. In addition to the orientation of radicals, concentration of radicals in each silica sample was a vital factor to be determined. Because the aim of this study was to compare the ^{29}Si DNP performance of the TEMPO-embedded silica samples to determine the favorable TEMPO distribution for DNP amplification, the concentration of TEMPO radicals between the investigated samples needs to be similar. The concentration of radicals was estimated based on the area under the curve calculated after double integration of the EPR spectra.²⁵ The area under the curve of the TEMPO sample was specifically chosen as a reference value for determining the radical-embedded silica samples (see Fig. S2[†]). Further details of the calculations are provided in the ESI.[†] The calculated TEMPO concentrations of the silica samples were summarized in Table S4,[†] which indicated that the radical concentrations were controlled at approximately 30 mM, which is suitable for conducting the ^{29}Si DNP experiments.

Following extensive physical and chemical characterizations, the prepared SiO_2 NPs were analyzed for their response to DNP. 60 mg of the NORMAL sample was mixed with 30 mM TEMPO solution to prepare a reference sample, which provided particles with exogenous surface-proximal electron spins for hyperpolarization. As other radical-embedded silica samples already contained TEMPO as an endogenous species, they were mixed with 40 μL of solvent mixture only, which consisted of dimethyl sulfoxide (DMSO) and D_2O (1 : 1 v/v). After preparation, samples were polarized in a home-built DNP instrument (5 T) at 3.3 K.⁴ For the ^{29}Si nuclear spin polarization build-up study to determine the time constant and overall signal enhancement level, all samples underwent DNP for 60 min and ^{29}Si MR signal was recorded using a 10° pulse applied once every 6 min. Fig. 4a and b show that the HOMO sample experienced the highest ^{29}Si intensity, which was 2.5-, 3.1- and 3.6-folds higher than those of the NORMAL, SHELL, and CORE samples, respectively. As expected, because radicals are only proximal to the outside surface of the NORMAL par-

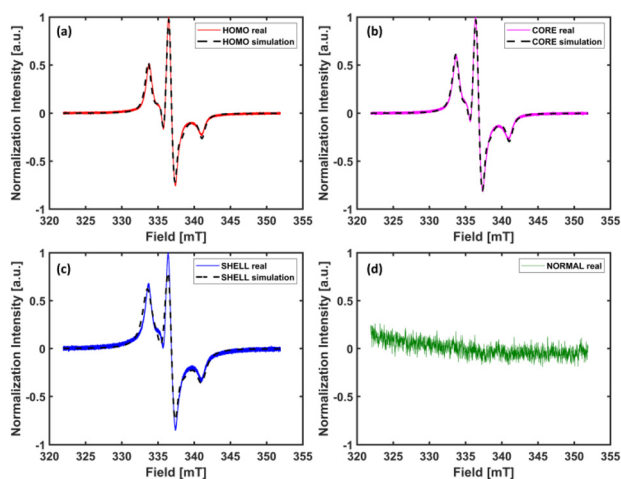


Fig. 3 Electron Paramagnetic Resonance (EPR) spectra of (a) HOMO, (b) CORE, (c) SHELL, and (d) NORMAL samples.

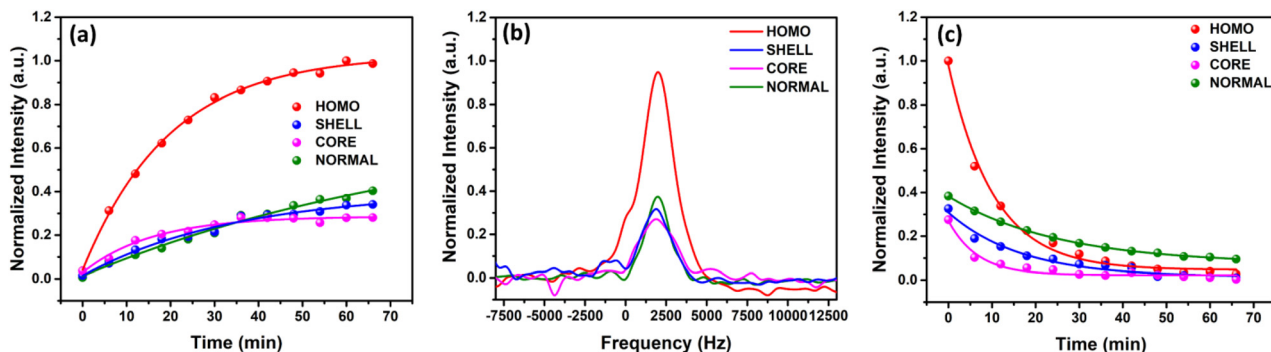


Fig. 4 DNP signals of ^{29}Si radicals-embedded silica NPs. (a) Build-up of hyperpolarized ^{29}Si signal over time. (b) Hyperpolarized ^{29}Si spectra at scan 12 (after 60 min of DNP). (c) Decay test of hyperpolarized ^{29}Si signal over time.

ticles, the extent of polarization on those particles' surface was limited compared to that of the HOMO sample, for which radicals were distributed homogeneously throughout the particles. This uniform radical distribution facilitated improved ^{29}Si polarization because of the higher number of ^{29}Si nuclei in close proximity to TEMPO. However, the SHELL and CORE samples (which also contained endogenous radicals in those regions of the particles) possessed approximately 1.7 and 2.4 times higher local radical densities than the HOMO sample, respectively (see ESI†). This may have resulted in the paramagnetic quenching of the DNP signal, consequently resulting in low intensities.^{20,21} Based on the build-up curves, the build-up time constants of all samples were determined using a mono-exponential function. Considering the fitted data, the CORE SiO_2 NP samples displayed the fastest build-up time constant (16 min) compared to that of NORMAL (83 min), SHELL (36 min), and HOMO (22 min) samples. In the case of radical-embedded silica samples, as the radical density increases, more ^{29}Si spins that are in close proximity to endogenous TEMPO are initially polarized; then, the enhanced signals are efficiently transferred to further ^{29}Si (in all directions) through spin diffusion. Meanwhile, the NORMAL sample used external radicals, which limited the induced spin diffusion to only be from the surface inward, resulting in a longer time for ^{29}Si MR signal build-up. While it was expected that the SHELL nanoparticles would exhibit faster polarization times compared to the HOMO particles because of the higher radical density that was localized to the nanoparticle shell, the opposite was observed. This behaviour presumably might be due to the polarization transfer pathways in the Q_4 sub-surface sites, which are largely distributed within the core of the particles. It is thought that these Q_4 sites significantly contribute to the build-up of ^{29}Si MR signals during DNP,²¹ and the rate of signal amplification depends on the proximity of these sub-surface sites to the embedded radical. In the case of the HOMO nanoparticles, the ^{29}Si nuclei in Q_4 sites can still be polarized directly by the unpaired electron of the nearby endogenous TEMPO radicals. However, in the SHELL sample, the number of Q_4 sites that are proximal to the shell-embedded radicals is significantly less than in the HOMO

case, requiring the spins to be polarized primarily through spin diffusion rather than directly through interaction with the radical. This observation on the build-up time constant of SHELL sample is quite interesting, additional researches need to be carried out to understand this phenomenon deeply.

Following the 1 h of DNP, the longitudinal decay of ^{29}Si polarization was measured using a series of 30° pulses with a 6 min delay between each to determine the sample T_1 value. For each scan, the $\sin(\alpha)$ of total longitudinal magnetization is converted to the observable transverse magnetization using a hard pulse with a fixed small flip angle, and $\cos(\alpha)$ of the longitudinal magnetization is preserved for the following scans. As a result of this fixed flip angle scheme, signal decays with a factor of $\lambda = (-\ln(\cos \alpha))/\Delta t$ where α is the flip angle and Δt is the delay time between scans. Based on the λ -factor, the real T_1 was calculated by equation as following, $1/T_{1,\text{real}} = 1/T_{1,\text{apparent}} - \lambda$. As shown in Fig. 4c, the longest T_1 was observed in the NORMAL sample (65 min), which was more than the T_1 of SHELL (31 min), HOMO (14 min), and CORE (8 min) samples. This tendency is consistent with the build-up time constant and can be explained by the short distances between the radicals and ^{29}Si nuclei in the particle core (for the HOMO and CORE particles), which is the primary limiter of T_1 in these samples.²¹ Because of the contribution of the Q_4 sites to the ^{29}Si signal enhancement, the concentration of radicals in the core region retained significant influence on the lifetime of the polarized signal. As the CORE particles possessed the highest density of radicals that were localized to the particle core (e.g., Q_4 sites), those particles exhibited the fastest depolarization rates (followed by the HOMO particles). While the radicals were not present in the core of the SHELL particles, they were embedded within the particle shells. This caused a faster depolarization rate in the SHELL particles compared to the NORMAL samples.

To demonstrate the signal enhancement obtained by DNP, one-dimensional (1D) ^{29}Si hyperpolarized spectra were recorded with and without microwave irradiations. Then, the DNP enhancement value of ^{29}Si (ϵ_{Si}) in the solid state was determined by comparing the integrated signal intensity of the hyperpolarized sample with the thermal equilibrium signal.

The direct DNP of ^{29}Si nuclei significantly boosts the intensity of silica samples (as shown in Fig. S3†). In particular, the DNP enhancement factors ϵ_{Si} of 49.4, 17.0, 14.1 and 19.9 are achieved corresponding to HOMO, SHELL, CORE and NORMAL particles. Although the lower local radical concentration of HOMO sample might induce the weaker polarization level of ^{29}Si nuclei, more ^{29}Si spins can be polarized in this case (as explained previously); therefore, overall enhancement factor of this sample is still highest. In contrast, higher local radical concentrations of both CORE and SHELL samples might provide stronger ^{29}Si polarization level from one ^{29}Si nucleus than the value of the HOMO sample; however, less nuclei would be polarized because the distance between radicals with ^{29}Si nuclei is shortened and nuclei which are located too close to the radicals will not be observed as a consequence of paramagnetic quenching effect.²⁶ Signal loss due to the paramagnetic effect can cause the significant smaller enhancement factors of CORE and SHELL in comparison with HOMO and even with the NORMAL sample. From the evidence above, the HOMO sample exhibited the highest polarization efficiency and has the best prospective to be used as an MRI probe.

This hyperpolarization study is the first to demonstrate that selectively radical-embedded SiO_2 NPs can be a potential probe for ^{29}Si MRI and provides valuable insights into an effective radical enrichment strategy using elaborate designs of SiO_2 NPs with different structures. Even though the homogeneous TEMPO-embedded SiO_2 NPs yielded a higher hyperpolarization enhancement, the relaxation rate of these particles was relatively fast, owing to the paramagnetic effect of the added radicals. Therefore, future studies will concentrate on extending the lifetime of the hyperpolarized state by regulating radical concentration²⁷ and adjusting the crystallinity of the SiO_2 nanoparticles *via* converting amorphous silica to α -quartz structure, which has T_1 relaxation time lasting for hours, to improve their applicability for *in vivo* ^{29}Si MRI.

In conclusion, we successfully synthesized selectively radical-embedded SiO_2 NPs with precise control over size, morphology, internal structure, and radical concentration. The polarization efficiency of the HOMO sample was significantly higher than that of the other selectively radical-embedded SiO_2 NPs, which yielded significantly higher ^{29}Si DNP intensity than the NORMAL sample with the same concentration of radicals added externally. This was due to the uniform distribution of radicals throughout the particles, which facilitated a better polarization with enhancement factor of 49.4. Overall, the results demonstrate that this radical enrichment approach can enhance the polarization extent in ^{29}Si DNP experiments, enabling us to probe not only the specific surface area but also the internal environment of the particle.

Author contributions

Q. S. L., Q. T. N., and J. K.: formal analysis, investigation software, prepared resources, and writing an original draft. J. K.:

prepared resources. N. W.: conceptualization and a writing – review & editing. J. H. S.: supervision, resources, and writing – review & editing. S. M.: supervision, project administration, and writing – review & editing. Y. L.: contributed as supervision, conceptualization, funding acquisition, methodology, project administration, and writing – review & editing.

Conflicts of interest

There are no conflicts to declare.

Acknowledgements

This research was supported by the National Research Foundation of Korea (NRF-2020R1A4A4079870 and NRF-2022R1A2C4001273).

References

- 1 P. C. van Zijl and N. N. Yadav, *Magn. Reson. Med.*, 2011, **65**, 927–948; T. B. Rodrigues, E. M. Serrao, B. W. Kennedy, D. E. Hu, M. I. Kettunen and K. M. Brindle, *Nat. Med.*, 2014, **20**, 93–97; C. Fu, J. Tang, A. Pye, T. Liu, C. Zhang, X. Tan, F. Han, H. Peng and A. K. Whittaker, *Biomacromolecules*, 2019, **20**, 2043–2050.
- 2 Y. Xu, Y. H. Li, Y. Wang, J. L. Cui, X. B. Yin, X. W. He and Y. K. Zhang, *Analyst*, 2014, **139**, 5134–5139; D. E. Korenchan, C. Taglang, C. von Morze, J. E. Blecha, J. W. Gordon, R. Sriram, P. E. Z. Larson, D. B. Vigneron, H. F. VanBrocklin, J. Kurhanewicz, D. M. Wilson and R. R. Flavell, *Analyst*, 2017, **142**, 1429–1433.
- 3 E. H. Suh, J. M. Park, L. Lumata, A. D. Sherry and Z. Kovacs, *Commun. Chem.*, 2020, **3**, 185; H. Park and Q. Wang, *Chem. Sci.*, 2022, **13**, 7378–7391.
- 4 S. Pudukalakatti, J. S. Enriquez, C. McCowan, S. Ramezani, J. S. Davis, N. M. Zacharias, D. Bourgeois, P. E. Constantinou, D. A. Harrington, D. Carson, M. C. Farach-Carson and P. K. Bhattacharya, *Wiley Interdiscip. Rev.: Nanomed. Nanobiotechnol.*, 2021, **13**, e1722; J. Kim, D. Jo, S. H. Yang, C. G. Joo, N. Whiting, S. Pudukalakatti, H. Seo, H. Y. Son, S. J. Min, P. Bhattacharya, Y. M. Huh, J. H. Shim and Y. Lee, *ACS Appl. Mater. Interfaces*, 2021, **13**, 56923–56930.
- 5 J. H. Ardenkjaer-Larsen, B. Fridlund, A. Gram, G. Hansson, L. Hansson, M. H. Lerche, R. Servin, M. Thaning and K. Golman, *Proc. Natl. Acad. Sci. U. S. A.*, 2003, **100**, 10158–10163; I. B. Moroz and M. Leskes, *Annu. Rev. Mater. Res.*, 2022, **52**, 25–55.
- 6 B. Gupta, Y. Zhu, B. Guan, P. J. Reece and J. J. Gooding, *Analyst*, 2013, **138**, 3593–3615; B. Xia, W. Zhang, J. Shi and S. Xiao, *Analyst*, 2013, **138**, 3629–3632; F. Tang, L. Li and D. Chen, *Adv. Mater.*, 2012, **24**, 1504–1534; Y. Chen, H. Chen and J. Shi, *Adv. Mater.*, 2013, **25**, 3144–3176.

- 7 M. C. Cassidy, H. R. Chan, B. D. Ross, P. K. Bhattacharya and C. M. Marcus, *Nat. Nanotechnol.*, 2013, **8**, 363–368.
- 8 J. W. Aptekar, M. C. Cassidy, A. C. Johnson, R. A. Barton, M. Lee, A. C. Ogier, C. Vo, M. N. Anahtar, Y. Ren, S. N. Bhatia, C. Ramanathan, D. G. Cory, A. L. Hill, R. W. Mair, M. S. Rosen, R. L. Walsworth and C. M. Marcus, *ACS Nano*, 2009, **3**, 4003–4008.
- 9 N. Whiting, J. Hu, J. V. Shah, M. C. Cassidy, E. Cressman, N. Z. Millward, D. G. Menter, C. M. Marcus and P. K. Bhattacharya, *Sci. Rep.*, 2015, **5**, 12842.
- 10 H. Seo, I. Choi, N. Whiting, J. Hu, Q. S. Luu, S. Pudakalakatti, C. McCowan, Y. Kim, N. Zacharias, S. Lee, P. Bhattacharya and Y. Lee, *ChemPhysChem*, 2018, **19**, 2143–2147.
- 11 J. H. Park, L. Gu, G. von Maltzahn, E. Ruoslahti, S. N. Bhatia and M. J. Sailor, *Nat. Mater.*, 2009, **8**, 331–336.
- 12 S. Milliken, A. N. Thiessen, I. T. Cheong, K. M. O'Connor, Z. Li, R. W. Hooper, C. J. T. Robidillo and J. G. C. Veinot, *Nanoscale*, 2021, **13**, 16379–16404.
- 13 J. G. Veinot, *Chem. Commun.*, 2006, 4160–4168.
- 14 D. R. Hristov, E. Mahon and K. A. Dawson, *Chem. Commun.*, 2015, **51**, 17420–17423.
- 15 I. L. Hsiao, S. Fritsch-Decker, A. Leidner, M. Al-Rawi, V. Hug, S. Diabate, S. L. Grage, M. Meffert, T. Stoeger, D. Gerthsen, A. S. Ulrich, C. M. Niemeyer and C. Weiss, *Small*, 2019, **15**, e1805400.
- 16 D. Lee, G. Monin, N. T. Duong, I. Z. Lopez, M. Bardet, V. Mareau, L. Gonon and G. De Paepe, *J. Am. Chem. Soc.*, 2014, **136**, 13781–13788.
- 17 Q. S. Luu, J. Kim, D. Jo, J. Jeong and Y. Lee, *Appl. Spectrosc. Rev.*, 2019, **55**, 476–490.
- 18 R. Harrabi, T. Halbritter, F. Aussenac, O. Dakhlaoui, J. van Tol, K. K. Damodaran, D. Lee, S. Paul, S. Hediger, F. Mentink-Vigier, S. T. Sigurdsson and G. De Paepe, *Angew. Chem., Int. Ed.*, 2022, **61**, e202114103.
- 19 A. S. Lilly Thankamony, O. Lafon, X. Lu, F. Aussenac, M. Rosay, J. Trébosc, H. Vezin and J.-P. Amoureux, *Appl. Magn. Reson.*, 2012, **43**, 237–250; R. Ciriminna, V. Pandarus, F. Béland and M. Pagliaro, *ChemCatChem*, 2018, **10**, 1731–1738.
- 20 M. de Oliveira Jr., K. Herr, M. Brodrecht, N. B. Haro-Mares, T. Wissel, V. Klimavicius, H. Breitzke, T. Gutmann and G. Buntkowsky, *Phys. Chem. Chem. Phys.*, 2021, **23**, 12559–12568; E. Besson, F. Ziarelli, E. Bloch, G. Gerbaud, S. Queyroy, S. Viel and S. Gastaldi, *Chem. Commun.*, 2016, **52**, 5531–5533; O. Lafon, A. S. Thankamony, M. Rosay, F. Aussenac, X. Lu, J. Trebosc, V. Bout-Roumazielles, H. Vezin and J. P. Amoureux, *Chem. Commun.*, 2013, **49**, 2864–2866.
- 21 U. Akbey, B. Altin, A. Linden, S. Ozcelik, M. Gradzielski and H. Oshkinat, *Phys. Chem. Chem. Phys.*, 2013, **15**, 20706–20716.
- 22 A. Clark, J. Sedhom, H. Elajaili, G. R. Eaton and S. S. Eaton, *Concepts Magn. Reson., Part A*, 2016, **45**, e21423; J. R. Biller and J. E. McPeak, *Appl. Magn. Reson.*, 2021, **52**, 1113–1139.
- 23 M. M. Roessler and E. Salvadori, *Chem. Soc. Rev.*, 2018, **47**, 2534–2553.
- 24 E. Bordignon, in *EPR Spectroscopy: Fundamentals and Methods*, ed. S. Stoll and D. Goldfarb, John Wiley & Sons Ltd., UK, 1st edn, 2018, ch. 14, pp. 277–301.
- 25 G. R. Eaton, S. S. Eaton, D. P. Barr and R. T. Weber, in *Quantitative EPR*, Springer Verlag, Germany, 1st edn, 2010, ch. 3, pp. 25–36.
- 26 A. J. Rossini, A. Zagdoun, M. Lelli, A. Lesage, C. Copéret and L. Emsley, *Acc. Chem. Res.*, 2013, **46**, 1942–1951.
- 27 J. Hu, N. Whiting and P. Bhattacharya, *J. Phys. Chem. C*, 2018, **122**, 10575–10581.